

Good Keypoints for the Two-View Geometry Estimation Problem

Konstantin Pakulev¹

Alexander Vakhitov²

Gonzalo Ferrer¹

¹Skolkovo Institute of Science and Technology

²Slamcore

<https://github.com/KonstantinPakulev/BoNeSS-ST>

Abstract

*Local features are essential to many modern downstream applications. Therefore, it is of interest to determine the properties of local features that contribute to the downstream performance for a better design of feature detectors and descriptors. In our work, we propose a new theoretical model for scoring feature points (keypoints) in the context of the two-view geometry estimation problem. The model determines two properties that a good keypoint for solving the homography estimation problem should have: be repeatable and have a small expected measurement error. This result provides key insights into why maximizing the number of correspondences doesn't always lead to better homography estimation accuracy. We use the developed model to design a method that detects keypoints that benefit the homography estimation introducing the **Bounded NeSS-ST (BoNeSS-ST)** keypoint detector. The novelty of BoNeSS-ST comes from (i) strong theoretical foundations, (ii) a more accurate keypoint scoring due to subpixel refinement and (iii) a cost designed for superior robustness to low saliency keypoints. As a result, BoNeSS-ST outperforms prior self-supervised local feature detectors in both planar homography and epipolar geometry estimation problems.*

1. Introduction

Establishing image-to-image correspondences is an essential component of modern Structure-from-Motion [30, 32, 39] (SfM) and visual SLAM [10, 13, 17, 23] (vSLAM) systems, which are used in areas of robotics and computer vision. Approaches for getting the correspondences between images can be classified into sparse, detector-free and dense. Sparse approaches [6, 19, 36] operate on images and produce a sparse set of features each of which is composed of a keypoint and its descriptor. Detector-free and dense approaches, on the other hand, operate on pairs of images. Former [33, 35, 42] directly output correspondences by performing coarse matching of feature maps followed by pixel-level refinement. Latter [8, 9, 34] produce a dense warp by utilizing a 4D-correlation volume.

Sparse approaches, due to their efficiency, present more interest for applications. Yet, to our knowledge, the influence of sparse features, keypoints in particular, on downstream performance is scarcely studied. This problem poses great significance since if we have a model describing what features are good for downstream tasks it will enable designing better keypoint detectors and descriptors, thereby, impacting numerous applications depending on them. In our work, we study the relationship between feature points and the two-view geometry estimation problem, which is encountered during the initialization of SfM and vSLAM systems. We aim to answer the following question: what properties of keypoints make them good for the downstream task of the two-view geometry estimation?

In Sec. 3.1 and Sec. 3.2, we answer the posed question for the case when two views are related by a planar homography. In Sec. 3.1, we demonstrate that the quality of a correspondence formed by a keypoint can be characterized by **the expected measurement error** (EME). In Sec. 3.2, we extend this result to assessing the quality of a keypoint itself. Specifically, we devise an extension of EME called β -EME that takes into account both the ability of the keypoint to form correspondences, *i.e.* **repeatability**, and the accuracy of formed correspondences, *i.e.* EME. We term β -EME in the score form as **the stability score**. We conclude that a keypoint is good for solving the homography estimation problem if it has a small expected measurement error and high repeatability. We point out an important implication that follows from that conclusion: more correspondences, more inliers or better classical metrics do not guarantee to improve the accuracy of the homography estimation.

In Sec. 3.3, we demonstrate that our mathematical model generalizes the notion of the stability score originally introduced in [25] and reveals the prior formulation to be one of the upper bounds. Building on this result, we improve the training mechanism of the NeSS-ST keypoint detector [25], which uses the stability score for generating the supervisory signal. We contribute by (i) deriving a tighter upper bound on the stability score (see Sec. 3.3), (ii) designing a more accurate supervisory signal generation procedure leveraging sub-pixel refinement (see Sec. 3.4) and (iii) proposing a

new cost function with high robustness to low saliency keypoints for training the neural network (see Sec. 3.5). We call our enhanced version of NeSS-ST trained in this manner **Bounded NeSS-ST (BoNeSS-ST)**.

In Sec. 4, we use BoNeSS-ST to experimentally verify our theoretical findings and show that they apply not only to the planar homography estimation problem but to the epipolar geometry estimation problem as well. BoNeSS-ST demonstrates downstream performance superior to its predecessor NeSS-ST [25] and other self-supervised keypoint detectors [3, 6, 15] on HEB [2], IMC-PT [12], MegaDepth [16] and ScanNet [5] establishing a new state of the art in two-view geometry estimation for self-supervised keypoint detectors.

2. Related Work

How to determine the quality of feature points? A classical approach to this problem is to use metrics such as repeatability [29], matching score [21] and mean matching accuracy [7], which capture the proportion of correct correspondences. For this reason, most learned keypoint detectors are trained to maximize these metrics [3, 6, 15, 24, 26] or the number of correspondences [36]. However, a comprehensive study of local features [12] demonstrated that classical metrics do not guarantee a faithful assessment of a method’s ability to perform well in downstream applications.

A relatively recent work [25] provided further evidence that high classical metrics do not necessarily mean better downstream performance. The authors introduced a novel keypoint quality measure, the stability score, that assesses the robustness of a keypoint to viewpoint transformations. The work showed that detectors trained using that measure demonstrate excellent performance in the epipolar geometry estimation task but have poor classical metrics. Yet, the work doesn’t provide deep insights into what causes such a difference in performance.

GMM-IKRS [28] is another work that explores the idea that repeatability alone is not a definitive measure of the quality of a keypoint. The authors suggest that apart from being repeatable a good keypoint should also have a small deviation, *i.e.* be detected close to the same position. The authors propose an interpretable score that allows to measure these properties via, correspondingly, robustness and deviation. GMM-IKRS utilizes the proposed scores in a framework for enhancing the performance of a keypoint detector that operates by identifying unreliable keypoints and refining the locations of reliable ones.

In our work, we develop a mathematical model that generalizes the stability score [25] and explains why it improves the downstream performance of keypoint detectors. We show that the stability score incorporates the properties of keypoints described by robustness and deviation [28] via a different characterization. Our findings provide an expla-

nation for the discrepancy between the downstream performance on the two-view geometry estimation task and repeatability that was observed in [12].

3. Method

3.1. Expected Measurement Error

We start by considering the nonlinear refinement of a homography estimate between two images I_1 and I_2 assuming given correspondences $\{k_i \leftrightarrow \bar{k}'_i\}_{i=1}^n$. The keypoint \bar{k}'_i on I_2 is known exactly. The keypoint k_i is a noisy measurement of the keypoint \bar{k}_i on I_1 such that $k_i = \bar{H}\bar{k}'_i$, where \bar{H} is the homography between the views. If we assume that the measurement error of \bar{k}_i obeys a Gaussian distribution $\mathcal{N}(\bar{0}, \bar{\Sigma}_i)$ then k_i can be viewed as a realization of a random variable $\bar{\mathbf{K}}_i \sim \mathcal{N}(\bar{k}_i, \bar{\Sigma}_i)$. Under this assumption, the maximum likelihood (ML) estimate \hat{H} of the homography \bar{H} is obtained by minimizing the transfer error [11] that is equivalent to maximizing the following log-likelihood:

$$\log f(\{k_i\}_{i=1}^n | H) = -\frac{1}{2} \sum_{i=1}^n \|k_i - H\bar{k}'_i\|_{\bar{\Sigma}_i}^2, \quad (1)$$

where H is an initial homography estimate.

The ML estimate \hat{H} is the optimal mapping (in terms of Eq. 1) between noise-free keypoints $\{\bar{k}'_i\}_{i=1}^n$ and measured keypoints $\{k_i\}_{i=1}^n$, which, however, is not guaranteed to be a close approximation of the homography \bar{H} [11]. For example, if $n = 4$ then \hat{H} is the exact mapping of noise-free keypoints $\{\bar{k}'_i\}_{i=1}^n$ to measured keypoints $\{k_i\}_{i=1}^n$. Asymptotically, as $n \rightarrow \infty$, one would expect $\frac{1}{n} \sum_{i=1}^n \|\bar{H}\bar{k}'_i - k_i\|_2$ to decrease [11]. In practice, n is limited by a keypoint budget; therefore, an estimate \hat{H} that approximates \bar{H} the best is achieved for the set $\{k_i \leftrightarrow \bar{k}'_i\}_{i=1}^n$ with the smallest total measurement error $\sum_{i=1}^n \|\bar{H}\bar{k}'_i - k_i\|_2$. Thus, if we have a model of $\mathcal{N}(\bar{k}_i, \bar{\Sigma}_i)$ then we can score correspondences benefitting the homography estimation according to individual $\|\bar{H}\bar{k}'_i - k_i\|_2$ by estimating $\mathbb{E}[\bar{\mathbf{K}}_i]$. In the following, we show that $\mathcal{N}(\bar{k}_i, \bar{\Sigma}_i)$ can be formulated as a distribution of projections of noisy measurements of the same visual structure as \bar{k}_i made in different views.

We define a noisy measurement (or a detection) as the application of a keypoint detector D to a random image patch $\bar{\mathbf{P}}_i \sim p(\bar{\mathbf{P}}_i)$ depicting an area around the image structure that \bar{k}_i corresponds to, where $p(\bar{\mathbf{P}}_i)$ is a probability density function (PDF) of the distribution of such patches. Next, we consider a random homography $\bar{\mathbf{H}}_i$ from $\bar{\mathbf{P}}_i$ to \bar{P}_i , which is a function of $\bar{\mathbf{P}}_i$ and \bar{P}_i , and define a random keypoint projection as $\bar{\mathbf{H}}_i D(\bar{\mathbf{P}}_i)$. One can notice that $\bar{\mathbf{H}}_i D(\bar{\mathbf{P}}_i)$, in general, follows a multimodal distribution since no keypoint detector D is guaranteed to produce

¹Here and in the following, we denote the transformation of a vector x by a homography H as Hx for readability.

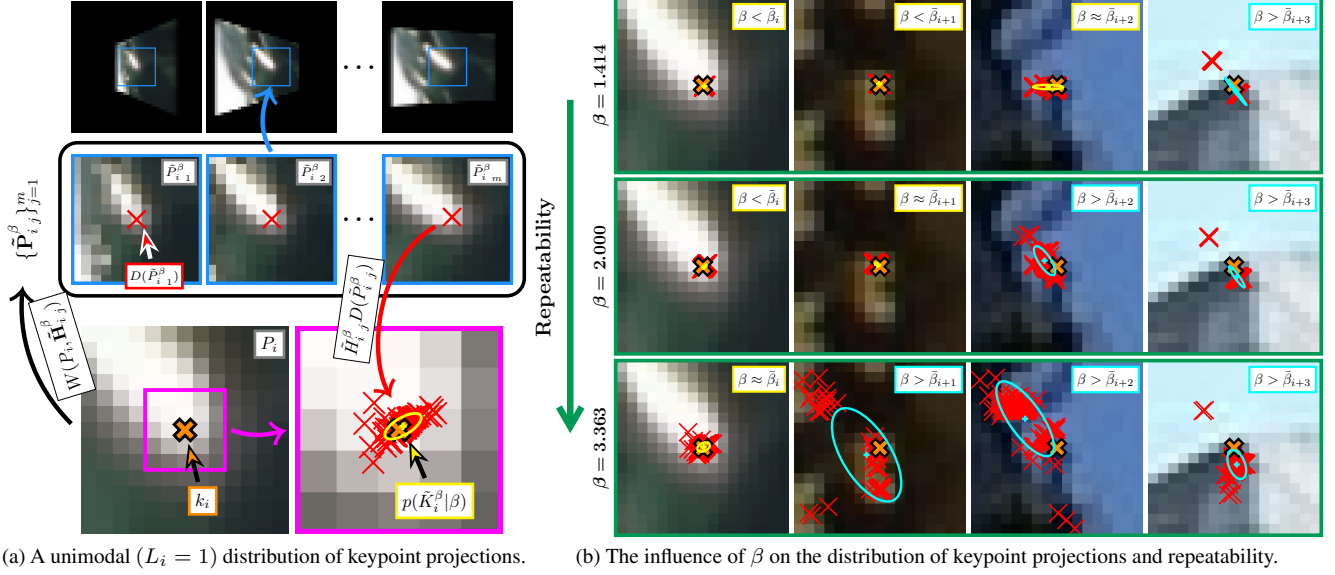


Figure 1. **(a)** We approximate $p(\{\tilde{K}_i^\beta\}_{l=1}^{L_i}|\beta)$ with $p(\{\tilde{K}_i^\beta\}_{l=1}^{L_i}|\beta)$ by using the distribution of synthetic patches with PDF $p(\tilde{P}_i|\beta)$. We generate random synthetic patches $\{\tilde{P}_i^\beta\}_{j=1}^m$ from P_i via a function W using random homographies $\{\tilde{H}_i^\beta\}_{j=1}^m$ (see Sec 6 in sup. mat.). **(b)** For small values of β , $p(\{\tilde{K}_i^\beta\}_{l=1}^{L_i}|\beta)$ is unimodal for most keypoints and can be approximated by a Gaussian \blacksquare . As β increases, $p(\{\tilde{K}_i^\beta\}_{l=1}^{L_i}|\beta)$ can no longer be approximated well by a Gaussian \blacksquare and remains unimodal only for repeatable keypoints. β -EME scores keypoints by both repeatability and EME, e.g. $\bar{\eta}_i > \bar{\eta}_{i+1}$ (see Eq. 3) but $\bar{\eta}_i^\beta < \bar{\eta}_{i+1}^\beta$ for $\beta = 3.363$ (see Eq. 4). Also, β -EME allows exploiting the prior knowledge about the difficulty of the transformation between two views, if available, to get more relevant EME. For example, if $\beta = 1.414$ is sufficient for keypoints to form correspondences then it is a better pick than $\beta = 3.363$. First, $p(\{\tilde{K}_i^\beta\}_{l=1}^{L_i}|\beta)$ for $\beta = 1.414$ can be well approximated by a Gaussian for more keypoints than for $\beta = 3.363$, which gives more keypoints with good EMEs. Second, the distribution of measurement projections includes only relevant viewpoint transformations. See Sec. 4.3 for more details.

measurements related to \bar{k}_i under arbitrary projective transformations. Therefore, we introduce a parameter β_i that constrains the sample space of \tilde{P}_i based on the difficulty of viewpoint transformations. We denote by $\tilde{P}_i^{\beta_i} \sim p(\tilde{P}_i|\beta_i)$ a random variable for which the sample space of corresponding $\tilde{H}_i^{\beta_i}$ is given as $\{\omega \in \Omega_{\tilde{H}_i} | d(I, \tilde{H}_i(\omega)) \leq \beta_i\}$, where d is a function that measures the difference in difficulty between two homographies, yielding:

$$\tilde{\mathbf{K}}_i^{\beta_i} = \tilde{\mathbf{H}}_i^{\beta_i} D(\tilde{P}_i^{\beta_i}). \quad (2)$$

Finally, we assume that $\tilde{\mathbf{K}}_i^{\beta_i} = \bar{\mathbf{K}}_i$ when $\beta_i = \bar{\beta}_i$ (see Fig. 1a) such that $\forall \beta_i > \bar{\beta}_i$ $\tilde{\mathbf{K}}_i^{\beta_i}$ follows a multimodal distribution (see Fig. 1b).

In practice, instead of noise-free keypoints $\{\bar{k}_i\}_{i=1}^n$ we have access only to their noisy measurements $\{k'_i\}_{i=1}^n$, where $k'_i = D(\tilde{P}_i')$, and $\tilde{P}_i' \in I_2$. So, we are interested in knowing $\|\tilde{H}k'_i - k_i\|_2$ - not $\|\tilde{H}k'_i - k_i\|_2$. But, unlike $\tilde{H}k'_i$, which is a constant independent of the choice of the second view I_2 , $\tilde{H}k'_i$ does depend on I_2 since k'_i is determined by the patch \tilde{P}_i' . Therefore, we consider the expectation of $\|\tilde{H}k'_i - k_i\|_2$ over all possible values of $\tilde{H}k'_i$:

$$\bar{\eta}_i = \mathbb{E}_{\tilde{\mathbf{K}}_i \sim \mathcal{N}(\bar{k}_i, \Sigma_i)} [\|\tilde{\mathbf{K}}_i - k_i\|_2]. \quad (3)$$

We term the measure in Eq. 3 **the expected measurement error (EME)**. EME quantifies the instability of measurements of the image structure related to \bar{k}_i and validates the fitness of the correspondence established by k_i for the homography estimation task.

3.2. Stability Score

While EME allows for scoring correspondences, it is not a good criterion for scoring keypoints because a keypoint with a good EME may not have a sufficient **repeatability** to form a correspondence. Therefore, we modify EME to also account for the repeatability of a keypoint. We notice that the model of EME does have a component that characterizes repeatability - $\bar{\beta}_i$. A keypoint k_i with a larger $\bar{\beta}_i$ is measured by D under more difficult transformations and, hence, is more repeatable (see Fig. 1b). Yet, EME doesn't reflect how large $\bar{\beta}_i$ is: given two keypoints with the same EME it is not possible to tell which one is more repeatable. Thus, to account for both repeatability and EME in a single measure, we take the expectation in Eq. 3 using a distribution of viewpoint transformations that is shared between all keypoints, which is achieved by letting $\beta_i = \beta$:

$$\bar{\eta}_i^\beta = \mathbb{E}_{\tilde{\mathbf{K}}_i^\beta \sim p(\{\tilde{K}_i^\beta\}_{l=1}^{L_i}|\beta)} [\|\tilde{\mathbf{K}}_i^\beta - k_i\|_2]. \quad (4)$$

We refer to the measure in Eq. 4 as β -EME. β -EME assesses the expected measurement error of a keypoint assuming apriori information β about the difficulty of the viewpoint transformation between two views. Each $\bar{\mathbf{K}}_i^\beta$ is assigned by β -EME into one of the two categories: (i) random variables following a unimodal distribution ($L_i = 1$ and $\beta \leq \bar{\beta}_i$) and (ii) random variables following a multimodal distribution ($L_i > 1$ and $\beta > \bar{\beta}_i$). If a keypoint falls into the first category then it meets the repeatability requirements set by β , and $\bar{\eta}_i^\beta$ is a faithful EME of k_i for the specified range of viewpoint transformations. Otherwise, the keypoint belongs to the second category and doesn't have the required repeatability from which it follows that $\bar{\eta}_i^\beta > \bar{\eta}_i$ because $\bar{\eta}_i^\beta$ is the expectation over a multimodal distribution (see Fig. 1b). Choosing the right β is important as keypoints with better repeatability are not necessarily the best according to EME (see Fig. 1b and Sec. 4.3). In practice, it is useful to represent β -EME in the form a score, which we call **the stability score**, defined on a half-open interval $(0, 1]$ as:

$$\bar{\Lambda}_i = e^{-\bar{\eta}_i^\beta}. \quad (5)$$

An important implication from the developed model is that having more correspondences, which generally means a higher number of inliers and better classical metrics, doesn't have to improve the accuracy of the homography estimation. According to our model, **a good keypoint** for solving the homography estimation problem **has to satisfy two properties**: be repeatable and have a small expected measurement error. We confirm this implication experimentally in Sec. 4 by using a keypoint detector enhanced with the stability score (see Sec. 3.5) and show that the implication also applies to the epipolar geometry estimation problem.

3.3. Bounded Stability Score

We now demonstrate that our model generalizes the notion of the stability score from [25]. Consider the following relation obtained by applying Jensen's inequality to Eq. 3:

$$\mathbb{E}[\|\bar{\mathbf{K}}_i - k_i\|_2]^2 \leq \mathbb{E}[\|\bar{\mathbf{K}}_i - k_i\|_2^2]. \quad (6)$$

When $\mathbb{E}[\|\bar{\mathbf{K}}_i - k_i\|_2] \geq 1$, it holds that $\mathbb{E}[\|\bar{\mathbf{K}}_i - k_i\|_2] \leq \mathbb{E}[\|\bar{\mathbf{K}}_i - k_i\|_2]^2$, and an upper bound on $\mathbb{E}[\|\bar{\mathbf{K}}_i - k_i\|_2]$ writes as:

$$\mathbb{E}[\|\bar{\mathbf{K}}_i - k_i\|_2] \leq \mathbb{E}[\|\bar{\mathbf{K}}_i - k_i\|_2^2]. \quad (7)$$

The right-hand side of Eq. 7 can be further decomposed as:

$$\begin{aligned} \mathbb{E}_{\bar{\mathbf{K}}_i \sim \mathcal{N}(\bar{k}_i, \bar{\Sigma}_i)}[\|\bar{\mathbf{K}}_i - k_i\|_2] &= \mathbb{E}[\|\bar{\mathbf{K}}_i - (\bar{k}_i + \delta_i)\|_2] \\ &= \mathbb{E}[\|\bar{\mathbf{K}}_i - \bar{k}_i\|_2] + \bar{\delta}_i^\top \bar{\delta}_i \quad (8) \\ &= \text{tr}(\bar{\Sigma}_i) + \bar{\delta}_i^\top \bar{\delta}_i, \end{aligned}$$

where $\bar{\delta}_i = k_i - \bar{k}_i$ is a constant. Then, assuming $k_i = \bar{k}_i$, the original formulation of the stability score [25] corresponds to an upper bound on Eq. 3:

$$\mathbb{E}[\|\bar{\mathbf{K}}_i - k_i\|_2] \leq \text{tr}(\bar{\Sigma}_i) \leq 2\|\bar{\Sigma}_i\|_2. \quad (9)$$

For practical purposes (see Sec. 3.5, Sec. 4.4 and Sec. 7 in sup. mat.), it is useful to have a bound that is exempt from limitations of Eq. 7, which requires $\mathbb{E}[\|\bar{\mathbf{K}}_i - k_i\|_2] \geq 1$, and Eq. 9, which additionally assumes $k_i = \bar{k}_i$ (doesn't generally hold). Therefore, we further improve the bound in Eq. 7 by applying the monotonic function \sqrt{x} to both sides of the inequality:

$$\mathbb{E}[\|\bar{\mathbf{K}}_i - k_i\|_2] \leq \sqrt{\mathbb{E}[\|\bar{\mathbf{K}}_i - k_i\|_2^2]}. \quad (10)$$

One can verify that Eq. 10 holds for every $\mathbb{E}[\|\bar{\mathbf{K}}_i - k_i\|_2]$ since $\mathbb{E}[\sqrt{x}] \leq \sqrt{\mathbb{E}[x]}$ from Jensen's inequality. We refer to the stability score calculated using a bound on Eq. 4 as **the bounded stability score**.

Eq. 8 offers an interpretable decomposition of bounds in Eq. 7, Eq. 9 and Eq. 10. Concretely, the term $\text{tr}(\bar{\Sigma}_i)$ is an upper bound on EME of \bar{k}_i and characterizes the spread of measurements of the image structure related to \bar{k}_i . The term $\bar{\delta}_i^\top \bar{\delta}_i$ is a squared Euclidian distance from \bar{k}_i and characterizes the negative log-likelihood of k_i to be close to a projection of a measurement, *i.e.* repeatability of k_i .

3.4. Synthetic Stability Score

Estimating the stability score or its bounds requires (i) drawing m samples $\{\bar{\mathbf{P}}_{i,j}^\beta\}_{j=1}^m \stackrel{\text{i.i.d.}}{\sim} p(\bar{P}_i|\beta)$ and (ii) producing measurements $\{D(\bar{P}_{i,j}^\beta)\}_{j=1}^m$ using realizations $\{\bar{P}_{i,j}^\beta\}_{j=1}^m$ of these samples. However, due to limitations of existing datasets with reconstructed correspondences, it is not possible to obtain samples of needed quality and in required quantities solely from real-world data [25]. Therefore, we adopt an approximation of Eq. 4 using a distribution of synthetic patches with PDF $p(\bar{P}_i|\beta)$, which we define via a procedure from [6, 25] (see Fig. 1a and Sec. 6 in sup. mat.):

$$\tilde{\eta}_i^\beta = \mathbb{E}_{\bar{\mathbf{K}}_i \sim p(\{\bar{K}_{i,l}^\beta\}_{l=1}^{L_i}|\beta)}[\|\bar{\mathbf{K}}_i^\beta - k_i\|_2]. \quad (11)$$

We denote the stability score calculated using Eq. 11 as $\tilde{\Lambda}_i$ and refer to it as **the synthetic stability score**.

To produce a measurement $D(\bar{P}_i^\beta)$ for the realization \bar{P}_i^β of a sampled synthetic view $\bar{\mathbf{P}}_i^\beta \sim p(\bar{P}_i|\beta)$, we propose the following procedure based on [25]. First, we apply the Shi-Tomasi detector [31] to \bar{P}_i^β getting a score patch \tilde{S}_i . Then, we apply non-maximum suppression to \tilde{S}_i and produce a candidate keypoint $\tilde{k}_i^{\text{cand}}$ by selecting the pixel with the maximum score from \tilde{S}_i . Next, we further refine $\tilde{k}_i^{\text{cand}}$ by

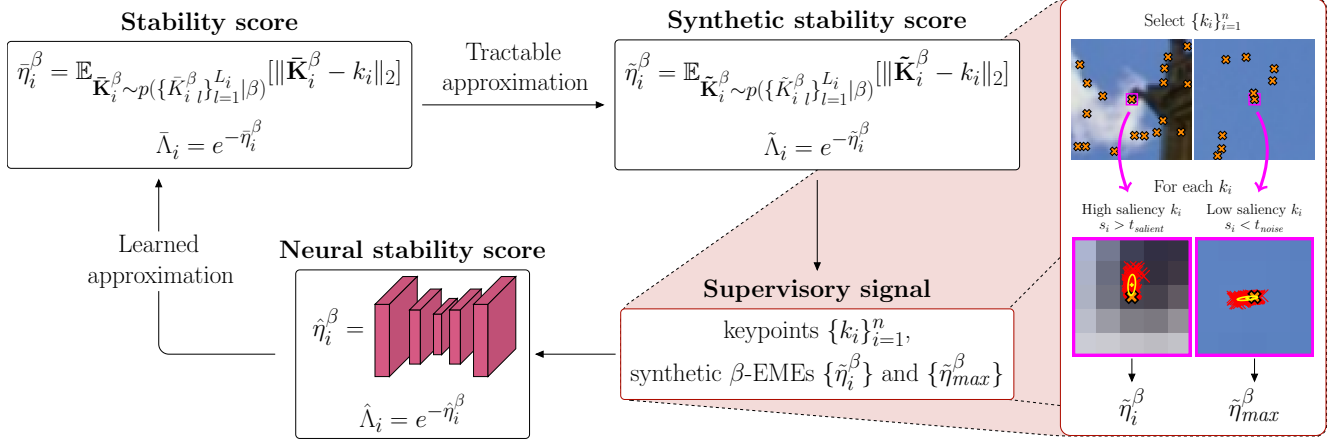


Figure 2. **Training pipeline.** We cannot provide an estimate of the stability score $\tilde{\Lambda}_i$ for a keypoint k_i because the distribution of keypoints projections with PDF $p(\{\tilde{K}_i^\beta\}_{l=1}^{L_i} | \beta)$ is intractable. Therefore, we learn an approximation of β -EME $\tilde{\eta}_i^\beta$ using the synthetic β -EME $\tilde{\eta}_i^\beta$ to create the supervisory signal. $\tilde{\eta}_i^\beta$ constitutes only a coarse approximation of $\tilde{\eta}_i^\beta$ and may yield erroneous estimates, e.g. for keypoints with low saliency $s_i < t_{noise}$. We replace such estimates with $\tilde{\eta}_{max}^\beta$ utilizing the knowledge that they are highly unlikely to be repeated.

assuming a continuous second-order approximation $\tilde{S}_i(\tilde{k}_i)$ of the Shi-Tomasi score \tilde{S}_i around \tilde{k}_i^{cand} [19, 25]:

$$\Delta \tilde{k}_i = -\frac{\partial^2 \tilde{S}_i^{-1}}{\partial \tilde{k}_i^2} \frac{\partial \tilde{S}_i}{\partial \tilde{k}_i}. \quad (12)$$

If $\det \frac{\partial^2 \tilde{S}_i}{\partial \tilde{k}_i^2} = 0$ or the condition number $\kappa(\frac{\partial^2 \tilde{S}_i}{\partial \tilde{k}_i^2}) \gg 1$ then a meaningful solution to Eq. 12 doesn't exist. Likewise, after applying non-maximum suppression, there might not be a suitable \tilde{k}_i^{cand} . Such image structures for which it is not possible to obtain reliable measurements are not likely to be repeated in practice. Therefore, for $\tilde{\eta}_i^\beta$ to be a better approximation of $\tilde{\eta}_i^\beta$, we output a measurement c with a large measurement error for these visual structures instead of relying on Shi-Tomasi. Thus, the complete measurement procedure is as follows:

$$D(\tilde{P}_i^\beta) = \begin{cases} \tilde{k}_i^{cand} + \Delta \tilde{k}_i & \det \frac{\partial^2 \tilde{S}_i}{\partial \tilde{k}_i^2} \neq 0 \text{ and} \\ & |\Delta \tilde{k}_i|_\infty < 0.5 \\ c & \text{otherwise} \end{cases}. \quad (13)$$

We demonstrate the importance of Eq. 13 in Sec. 4.4.

The distribution with PDF $p(\tilde{P}_i | \beta)$ features only viewpoint changes of the neighborhood of \tilde{k}_i , so $\tilde{\eta}_i^\beta$, the synthetic β -EME, can be vastly different from the true value $\tilde{\eta}_i^\beta$ for some of the keypoints (see Fig. 2). This flaw limits using the synthetic stability score in practice.

3.5. Bounded Neural Stability Score

To overcome the limitations of the synthetic stability score, the authors in [25] use $\tilde{\eta}_i^\beta$ as a part of the supervisory signal to learn a more accurate approximation $\hat{\eta}_i^\beta$ of $\tilde{\eta}_i^\beta$ from the

data via a neural network² (see Fig. 2). Hence, the stability score $\hat{\Lambda}_i$ calculated using $\hat{\eta}_i^\beta$ is referred to as **the neural stability score** (NeSS). The neural approximation $\hat{\eta}_i^\beta$ is learned by exploiting the observation that an erroneous $\tilde{\eta}_i^\beta$ is highly likely to come from a low-saliency area. So, a keypoint k_i with a Shi-Tomasi score s_i is used as the ground truth for learning $\hat{\eta}_i^\beta$ only if $s_i > t_{salient}$, where $t_{salient}$ is a threshold. Thus, this approach doesn't penalize keypoints with low saliency directly because some of them do correspond to meaningful signals and relies on the structure of the neural network to impede fitting the parameters to noise [37].

Based on our mathematical model (see Sec. 3.2), we propose an improvement to the supervisory signal generation procedure for learning NeSS. Consider a keypoint with extremely low saliency such that $\tilde{\eta}_i \approx 0$, e.g. image noise. For this keypoint, small changes in the realization of \tilde{P}_i^β yield measurements related to different image structures each of which is unlikely to be repeated. Therefore, when calculating a synthetic approximation of $\tilde{\eta}_i^\beta$ for such a keypoint, we can employ Eq. 13 to return c for each measurement. Then, $\tilde{\eta}_i^\beta$ calculated from projections of these measurements equals $\tilde{\eta}_{max}^\beta$ - the maximum possible value of β -EME. To get such low-saliency keypoints for training, we consider an extra threshold t_{noise} such that $t_{noise} \ll t_{salient}$ and use a keypoint k_i as the ground truth if $s_i < t_{noise}$. This allows us to provide ground truth for more keypoints compared to NeSS-ST [25] and improve the training (see Fig. 2 and Sec. 4.4).

The training of the neural network is organized as follows. Given an image, we use the Shi-Tomasi detector

²Since our approach generalizes the one proposed in [25], we use our notation for explaining NeSS for consistent narrative.

for obtaining positions of all keypoints for which $s_i > t_{salient} \vee s_i < t_{noise}$. Then, we employ the neural network with the so-far-trained weights [3, 24, 25, 36] to predict $\hat{\eta}_i^\beta$ for each pixel of the image and select n keypoints $\{k_i\}_{i=1}^n$ among keypoints detected by Shi-Tomasi with the highest $\{\hat{\eta}_i^\beta\}_{i=1}^n$. Next, we apply the bound from Eq. 10 to Eq. 11 and use it to estimate $\{\tilde{\eta}_i^\beta\}_{i=1}^n$ for $\{k_i\}_{i=1}^n$. We process $\{\tilde{\eta}_i^\beta\}_{i=1}^n$ to prepare the ground truth by replacing estimates for which $s_i < t_{noise}$ with $\tilde{\eta}_{max}^\beta$. Finally, we train the neural network using the following objective:

$$L = \frac{\sum_{s_i > t_{salient}} (\hat{\eta}_i^\beta - \tilde{\eta}_i^\beta)^2 + \sum_{s_i < t_{noise}} (\hat{\eta}_i^\beta - \tilde{\eta}_{max}^\beta)^2}{n}. \quad (14)$$

We call our detector BoNeSS-ST because it scores keypoints detected by Shi-Tomasi (ST) using **the bounded neural stability score** (BoNeSS), which is calculated using the inference of the neural network. Refer to Sec. 7 in sup. mat. for the details about the design of the detector.

4. Experiments

We conduct the evaluation using the two-view geometry estimation task and classical metrics to support the statements of our theoretical model and highlight the importance of design choices made in Sec. 3. We compare BoNeSS-ST with Shi-Tomasi [31] and NeSS-ST [25] for a better illustration of the advantages that a finer scoring of keypoints brings. Note, that all three methods rely on **exactly the same** keypoints provided by Shi-Tomasi but score and, hence, top-k select them differently. The evaluation also includes other baseline and state-of-the-art methods: SIFT [19], SuperPoint [6], R2D2 [26], Key.Net [3], DISK [36], REKD [15].

4.1. Evaluation on the Two-View Geometry Estimation Task

We demonstrate that the stability score enhances the downstream performance of a keypoint detector on the homography estimation task as stated in Sec. 3.2 by evaluating on the planar homography estimation benchmark - HEB. HEB is a dataset of landmarks photos with a focus on planar surfaces. The dataset features strong viewpoint and illumination changes totaling 169k test image pairs with 4.8k unique test images. Additionally, we study how the results of Sec. 3.2 apply to the epipolar geometry estimation problem by evaluating on IMC-PT [12], MegaDepth [16] and ScanNet [5] datasets.

A proper evaluation of keypoint detectors on downstream tasks requires using a single keypoint descriptor for all methods [3, 21, 25, 38, 41]. We use the DISK descriptor [36] on IMC-PT [12] and MegaDepth [16] and the HardNet [22] descriptor - on ScanNet [5]. For HEB [2], we also choose DISK due to its good performance. Another impor-

tant component of the evaluation is choosing hyperparameters such as Lowe ratio [19] and inlier threshold for each method [12]. For this reason, we slightly change the hyperparameter tuning procedure from [25] to obtain better hyperparameters. Once initial values of hyperparameters are found using a greedy approach from [12], we do a grid search in their neighborhood following [2]. See Sec. 8 in sup. mat. for more details about the evaluation protocol.

Results. The results in Table 1 show that replacing the criterion for scoring keypoints detected by the Shi-Tomasi detector with the stability score (NeSS-ST and BoNeSS-ST) yields significant improvements in both planar homography estimation task and epipolar geometry estimation task. Table 1 also demonstrates that the number of inliers is not a definitive measure of the quality of the two-view geometry estimation accuracy. The results indicate that apart from their numbers there is an equally important ‘‘intrinsic’’ property of inliers that influences mAA. In Sec. 4.3, we provide evidence that this intrinsic property is the expected measurement error. Thus, the presented experimental data align with the conclusion of Sec. 3.2 about the properties of keypoints that are good for the homography estimation problem and show that the same considerations apply to the epipolar geometry estimation problem. Refer to Sec. 9.1 in sup. mat. for more evaluation results.

BoNeSS-ST establishes a new state of the art among self-supervised keypoint detectors in the two-view geometry estimation task by outperforming all its competitors: SuperPoint [6], Key.Net [3], REKD [15] and NeSS-ST [25]. A good performance of Shi-Tomasi, SIFT, SuperPoint, NeSS-ST and BoNeSS-ST demonstrates that the classical definition of a keypoint [18] (a blob or a corner) is still highly competitive. For this reason, we believe there is a potential to continue developing hybrid learned-classical approaches [3, 25] and approaches inspired by the classical definition of a keypoint [6].

4.2. Evaluation with Classical Metrics

We provide further support to the conclusion of Sec. 3.2 by evaluating on the HPatches dataset [1] using classical metrics: repeatability [29] and mean matching accuracy (MMA) [7, 20]. We use the DISK descriptor [36] for this dataset as it shows state-of-the-art performance there.

Results. Table 2 demonstrates a significant discrepancy in the ranking of the methods compared to Table 1, *e.g.* Shi-Tomasi is superior to NeSS-ST and BoNeSS-ST according to classical metrics. Thus, not only the number of inliers but also the proportion of correct matches, which is characterized by classical metrics, is not a definitive measure of the ability of a method to perform well in the two-view geometry estimation task. Nevertheless, similarly to the number of

Method	Self-sup.	HEB [2]		IMC-PT [12]			MegaDepth [16]			ScanNet [5]		
		R	NI	R	t	NI	R	t	NI	R	t	NI
SIFT [19]	NA	0.182	49.2	0.713	0.387	181.2	0.845	0.295	383.6	0.576	0.195	106.9
SuperPoint [6]	✓	0.225	55.7	0.709	0.370	114.5	0.875	0.321	395.4	0.611	0.212	83.1
R2D2 [26]	✗	0.232	65.9	0.750	0.408	250.2	0.873	0.313	452.0	0.643	0.235	166.3
Key.Net [3]	✓	0.202	54.4	0.677	0.327	136.5	0.848	0.276	384.4	0.603	0.210	84.6
DISK [36]	✗	0.249	127.5	0.817	0.487	470.3	0.884	0.323	622.3	0.525	0.161	138.9
REKD [15]	✓	0.213	55.7	0.605	0.269	128.2	0.856	0.271	396.1	0.453	0.139	141.5
Shi-Tomasi [31]	NA	0.196	57.0	0.751	0.426	215.0	0.864	0.311	429.0	0.568	0.194	148.9
NeSS-ST [25]	✓	0.229	44.0	0.769	0.446	158.4	0.878	0.338	299.2	0.621	0.218	106.8
BoNeSS-ST	✓	0.230	54.7	0.788	0.457	217.1	0.887	0.339	362.9	0.652	0.235	162.5

Table 1. Evaluation on the two-view geometry estimation task. We report relative pose rotation (R) and translation (t) mAA [12, 40] for a 10-degree threshold as well as the number of inliers (NI). We denote self-supervised methods by ✓. The best results are in **red**, the 2nd best - in **green** and the 3rd best - in **blue**.

Method	Self-sup.	Overall		Illumination		Viewpoint	
		Rep.	MMA	Rep.	MMA	Rep.	MMA
SIFT [19]	NA	0.495	0.747	0.521	0.793	0.472	0.705
SuperPoint [6]	✓	0.616	0.777	0.767	0.816	0.475	0.740
R2D2 [26]	✗	0.549	0.755	0.597	0.801	0.505	0.711
Key.Net [3]	✓	0.573	0.741	0.773	0.788	0.387	0.697
DISK [36]	✗	0.547	0.768	0.592	0.817	0.504	0.723
REKD [15]	✓	0.548	0.684	0.747	0.761	0.364	0.612
Shi-Tomasi [31]	NA	0.573	0.777	0.557	0.815	0.588	0.742
NeSS-ST [25]	✓	0.401	0.713	0.431	0.738	0.372	0.690
BoNeSS-ST	✓	0.476	0.757	0.511	0.798	0.444	0.719

Table 2. Evaluation on HPatches [1] using classical metrics. We report repeatability (Rep.) [29] and MMA [7, 20] for a 3-pixel threshold. We denote self-supervised methods by ✓. The best results are in **red**.

inliers, classical metrics can strongly correlate with the improvements in downstream performance, which can be seen by comparing the performance of NeSS-ST and BoNeSS-ST. This, again, hints at the existence of some intrinsic property of a keypoint (see Sec. 4.3). Refer to Sec. 9.2 in sup. mat. for more evaluation results.

4.3. The Intrinsic Property of a Keypoint

The experimental data in Sec. 4.1 and Sec. 4.2 indicate the existence of the intrinsic property of a keypoint that is necessary to account for to get accurate two-view geometry estimates. We provide conclusive evidence that the expected measurement error is that property. To demonstrate this, we sweep the parameter β , which controls repeatability in our model (see Sec. 3.2), and study the effect of changing it on the performance. For this experiment, we trained NeSS-ST using our pipeline from scratch, so its performance with $\beta = 2.0$ differs from the one reported in Table 1.

Results. Table 3 shows that the best relative pose mAA for both detectors is achieved when β constitutes a reasonable guess on the difficulty of viewpoint transformations between dataset views: $\beta = 2.000$ for NeSS-ST and $\beta = 1.414$ for BoNeSS-ST. This ensures that keypoints have sufficient repeatability for forming enough matches. Increasing β past these values shifts the scoring priority to more repeatable keypoints but comes with a slight decrease in the downstream performance due to how β -EME (see Eq. 4) is constructed. Specifically, as β increases, the number of keypoints for which $\bar{\mathbf{K}}_i^\beta$ follows a unimodal distribution of measurements related to k_i decreases. Thus, we gradually lose keypoints with good EMEs for which the Gaussian assumption is no longer fulfilled due to $\beta > \bar{\beta}_i$ (see Fig. 1b). Nevertheless, we get to retain the major portion of the performance because the stability score for repeatable keypoints is high only if they have good EMEs. For $\beta = 3.363$, BoNeSS-ST approaches Shi-Tomasi in repeatability on viewpoint sequences of HPatches (see Table 2) while keeping superior mAA compared to it on IMC-PT (see Table 1). This means that some repeatable keypoints detected by the Shi-Tomasi detector present a suboptimal choice for the downstream task (see Fig. 3). Thus, accounting for the expected measurement error is essential for having a good two-view geometry estimation performance, which supports the conclusion of Sec. 3.2.

4.4. Ablation Study

We study the contribution of each of the following components on the downstream performance of BoNeSS-ST: (i) a tighter upper bound on β -EME (see Eq. 10), (ii) a more accurate measurement procedure (see Eq. 13) and (iii) a better supervisory signal generation procedure (see Sec. 3.5). Like in Sec. 4.3, we use the retained NeSS-ST model.

β	NeSS-ST [25]					BoNeSS-ST				
	R	t	NI	Rep.	MMA	R	t	NI	Rep.	MMA
1.414	0.773	0.448	162.0	0.348	0.688	0.787	0.461	208.3	0.422	0.714
1.681	0.776	0.451	170.0	0.360	0.692	0.787	0.459	209.2	0.422	0.710
2.000	0.778	0.451	174.2	0.384	0.703	0.788	0.457	217.1	0.444	0.719
2.378	0.773	0.449	181.7	0.403	0.703	0.782	0.458	212.2	0.463	0.720
2.828	0.781	0.447	198.9	0.464	0.720	0.789	0.451	228.4	0.485	0.725
3.363	-	-	-	-	-	0.785	0.453	209.6	0.503	0.726

Table 3. Ablation study of the influence of the parameter β on the performance on IMC-PT [12] and viewpoint sequences of HPatches [1]. For IMC-PT, we report relative pose rotation (R) and translation (t) mAA [12, 40] for a 10-degree threshold as well as the number of inliers (NI). For viewpoint sequences of HPatches, we report repeatability (Rep.) [29] and MMA [7, 20] for a 3-pixel threshold. The best results are in **red**.

β -EME	$t_{salient}$ [25]			$t_{salient}$ [25] + Eq. 13			$t_{salient}$ [25] + t_{noise}			$t_{salient}$ [25] + Eq. 13 + t_{noise}		
	R	t	NI	R	t	NI	R	t	NI	R	t	NI
$\ \bar{\Sigma}_i\ _2$ [25]	0.778	0.451	174.2	0.781	0.453	191.7	0.780	0.456	206.2	0.780	0.459	208.9
$\text{tr}(\bar{\Sigma}_i) + \bar{\delta}_i^T \bar{\delta}_i$	0.782	0.454	187.8	0.777	0.457	185.9	0.783	0.454	216.1	0.785	0.455	212.5
$\sqrt{\text{tr}(\bar{\Sigma}_i) + \bar{\delta}_i^T \bar{\delta}_i}$	0.765	0.451	169.8	0.776	0.455	179.4	0.780	0.460	202.3	0.788	0.457	217.1
$\mathbb{E}[\ \bar{\mathbf{K}}_i - k_i\ _2]$	0.777	0.450	187.1	0.777	0.455	183.8	0.785	0.456	206.3	0.787	0.458	215.2

Table 4. Ablation study of the influence of design choices of BoNeSS-ST proposed in Sec. 3 on the downstream performance on IMC-PT [12]. We report rotation (R) and translation (t) mAA [12, 40] for a 10-degree threshold as well as the number of inliers (NI). The best results are in **red**. Note, that the best values in columns R and t are selected according to a total sum of rotation and translation mAA.

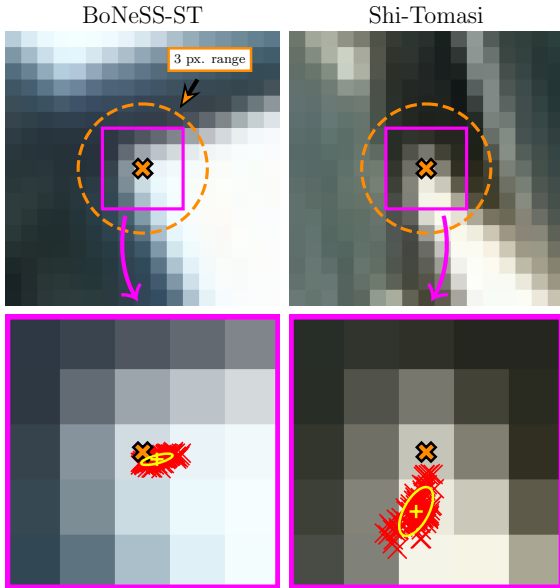


Figure 3. The best keypoints according to the scoring of BoNeSS-ST and Shi-Tomasi detectors. While both keypoints are repeatable within the 3-pixel threshold, they have noticeably different quality in terms of the expected measurement error.

Results. The results in Table 4 show that the proposed supervisory signal generation procedure that utilizes t_{noise} and the measurement procedure in Eq. 13 enhance the downstream performance when applied both separately and together. Additionally, they demonstrate that t_{noise} is necessary for obtaining better results for tighter bounds.

5. Conclusion

In this work, we developed a mathematical model that describes the properties that a good keypoint for the homography estimation problem should have: repeatability and expected measurement error. The main implication from the presented model is that having more correspondences, inliers or better classical metrics does not always lead to superior two-view geometry estimates. We experimentally verified this claim and demonstrated that accounting for the expected measurement error enables retaining good downstream performance for keypoints with different repeatability. Additionally, we showed that the developed theory generalizes the notion of the stability score presented in the prior work and used the theory to improve the training of the NeSS-ST detector [25]. Titled BoNeSS-ST, our enhanced keypoint detector has good generalization and demonstrates state-of-the-art performance on multiple datasets and tasks.

References

- [1] Vassileios Balntas, Karel Lenc, Andrea Vedaldi, and Krystian Mikolajczyk. Hpatches: A benchmark and evaluation of handcrafted and learned local descriptors. In *CVPR*, pages 5173–5182, 2017. 6, 7, 8, 19
- [2] Daniel Barath, Dmytro Mishkin, Michal Polic, Wolfgang Förstner, and Jiri Matas. A large-scale homography benchmark. In *Proceedings of the IEEE/CVF Conference on Computer Vision and Pattern Recognition*, pages 21360–21370, 2023. 2, 6, 7, 12, 13, 14, 17
- [3] Axel Barroso-Laguna, Edgar Riba, Daniel Ponsa, and Krystian Mikolajczyk. Key. net: Keypoint detection by handcrafted and learned cnn filters. In *CVPR*, pages 5836–5844, 2019. 2, 6, 7, 13
- [4] Ondrej Chum, Tomas Werner, and Jiri Matas. Two-view geometry estimation unaffected by a dominant plane. In *CVPR*, pages 772–779. IEEE, 2005. 13
- [5] Angela Dai, Angel X Chang, Manolis Savva, Maciej Halber, Thomas Funkhouser, and Matthias Nießner. Scannet: Richly-annotated 3d reconstructions of indoor scenes. In *CVPR*, pages 5828–5839, 2017. 2, 6, 7, 11, 12, 13, 16, 19
- [6] Daniel DeTone, Tomasz Malisiewicz, and Andrew Rabinovich. Superpoint: Self-supervised interest point detection and description. In *Proceedings of the IEEE conference on computer vision and pattern recognition workshops*, pages 224–236, 2018. 1, 2, 4, 6, 7, 11, 13, 17
- [7] Mihai Dusmanu, Ignacio Rocco, Tomas Pajdla, Marc Pollefeys, Josef Sivic, Akihiko Torii, and Torsten Sattler. D2-net: A trainable cnn for joint detection and description of local features. *arXiv preprint arXiv:1905.03561*, 2019. 2, 6, 7, 8, 13, 19
- [8] Johan Edstedt, Ioannis Athanasiadis, Mårten Wadenbäck, and Michael Felsberg. DKM: Dense kernelized feature matching for geometry estimation. In *IEEE Conference on Computer Vision and Pattern Recognition*, 2023. 1
- [9] Johan Edstedt, Qiyu Sun, Georg Bökman, Mårten Wadenbäck, and Michael Felsberg. RoMa: Robust Dense Feature Matching. *IEEE Conference on Computer Vision and Pattern Recognition*, 2024. 1
- [10] Christian Forster, Matia Pizzoli, and Davide Scaramuzza. Svo: Fast semi-direct monocular visual odometry. In *2014 IEEE international conference on robotics and automation (ICRA)*, pages 15–22. IEEE, 2014. 1
- [11] Richard Hartley and Andrew Zisserman. *Multiple view geometry in computer vision*. Cambridge university press, 2003. 2
- [12] Yuhe Jin, Dmytro Mishkin, Anastasiia Mishchuk, Jiri Matas, Pascal Fua, Kwang Moo Yi, and Eduard Trulls. Image matching across wide baselines: From paper to practice. *International Journal of Computer Vision*, 129(2):517–547, 2021. 2, 6, 7, 8, 11, 12, 13, 14, 15, 16, 17, 18, 19
- [13] Georg Klein and David Murray. Parallel tracking and mapping for small ar workspaces. In *2007 6th IEEE and ACM international symposium on mixed and augmented reality*, pages 225–234. IEEE, 2007. 1
- [14] Laurent Kneip and Paul Furgale. Opengv: A unified and generalized approach to real-time calibrated geometric vision. pages 1–8. IEEE, 2014. 13
- [15] Jongmin Lee, Byungjin Kim, and Minsu Cho. Self-supervised equivariant learning for oriented keypoint detection. In *CVPR*, pages 4847–4857, 2022. 2, 6, 7, 13
- [16] Zhengqi Li and Noah Snavely. Megadepth: Learning single-view depth prediction from internet photos. In *CVPR*, pages 2041–2050, 2018. 2, 6, 7, 11, 13, 18
- [17] Hyon Lim, Jongwoo Lim, and H Jin Kim. Real-time 6-dof monocular visual slam in a large-scale environment. In *2014 IEEE international conference on robotics and automation (ICRA)*, pages 1532–1539. IEEE, 2014. 1
- [18] Tony Lindeberg. Feature detection with automatic scale selection. *IJCV*, 30(2):79–116, 1998. 6
- [19] David G Lowe. Distinctive image features from scale-invariant keypoints. *IJCV*, 60(2):91–110, 2004. 1, 5, 6, 7, 12, 13
- [20] Krystian Mikolajczyk and Cordelia Schmid. A performance evaluation of local descriptors. *IEEE transactions on pattern analysis and machine intelligence*, 27(10):1615–1630, 2005. 6, 7, 8, 13, 19
- [21] Krystian Mikolajczyk, Tinne Tuytelaars, Cordelia Schmid, Andrew Zisserman, Jiri Matas, Frederik Schaffalitzky, Timor Kadir, and L Van Gool. A comparison of affine region detectors. *IJCV*, 65:43–72, 2005. 2, 6
- [22] Anastasiia Mishchuk, Dmytro Mishkin, Filip Radenovic, and Jiri Matas. Working hard to know your neighbor’s margins: Local descriptor learning loss. *NeurIPS*, 30, 2017. 6
- [23] Raul Mur-Artal, Jose Maria Martinez Montiel, and Juan D Tardos. ORB-SLAM: a versatile and accurate monocular SLAM system. 31(5):1147–1163, 2015. 1
- [24] Yuki Ono, Eduard Trulls, Pascal Fua, and Kwang Moo Yi. LF-Net: Learning local features from images. *NeurIPS*, 31, 2018. 2, 6
- [25] Konstantin Pakulev, Alexander Vakhitov, and Gonzalo Ferrer. Ness-st: Detecting good and stable keypoints with a neural stability score and the shi-tomasi detector. In *Proceedings of the IEEE/CVF International Conference on Computer Vision*, pages 9578–9588, 2023. 1, 2, 4, 5, 6, 7, 8, 11, 12, 13
- [26] Jerome Revaud, Cesar De Souza, Martin Humenberger, and Philippe Weinzaepfel. R2d2: Reliable and repeatable detector and descriptor. In *NeurIPS*. Curran Associates, Inc., 2019. 2, 6, 7, 13
- [27] Olaf Ronneberger, Philipp Fischer, and Thomas Brox. U-net: Convolutional networks for biomedical image segmentation. pages 234–241. Springer, 2015. 11
- [28] Emanuele Santellani, Martin Zach, Christian Sormann, Matia Rossi, Andreas Kuhn, and Friedrich Fraundorfer. Gmm-ikrs: Gaussian mixture models for interpretable keypoint refinement and scoring. In *European Conference on Computer Vision*, pages 77–93. Springer, 2024. 2, 12
- [29] Cordelia Schmid, Roger Mohr, and Christian Bauckhage. Comparing and evaluating interest points. In *Sixth International Conference on Computer Vision (IEEE Cat. No. 98CH36271)*, pages 230–235. IEEE, 1998. 2, 6, 7, 8, 13, 19

- [30] Johannes L Schonberger and Jan-Michael Frahm. Structure-from-motion revisited. In *CVPR*, pages 4104–4113, 2016. [1](#)
- [31] Jianbo Shi and Tomasi. Good features to track. In *CVPR*, pages 593–600, 1994. [4](#), [6](#), [7](#), [13](#)
- [32] Noah Snavely. Scene reconstruction and visualization from internet photo collections: A survey. *IPSI Transactions on Computer Vision and Applications*, 3:44–66, 2011. [1](#)
- [33] Jiaming Sun, Zehong Shen, Yuang Wang, Hujun Bao, and Xiaowei Zhou. LoFTR: Detector-free local feature matching with transformers. In *2021 IEEE/CVF Conference on Computer Vision and Pattern Recognition (CVPR)*, pages 8918–8927. IEEE. [1](#)
- [34] Prune Truong, Martin Danelljan, Luc Van Gool, and Radu Timofte. Learning accurate dense correspondences and when to trust them. In *Proceedings of the IEEE/CVF conference on computer vision and pattern recognition*, pages 5714–5724, 2021. [1](#)
- [35] Khang Truong Giang, Soohwan Song, and Sungho Jo. TopicFM: Robust and Interpretable Topic-Assisted Feature Matching. *Proceedings of the AAAI Conference on Artificial Intelligence*, 37(2):2447–2455, 2023. [1](#)
- [36] Michał Tyszkiewicz, Pascal Fua, and Eduard Trulls. Disk: Learning local features with policy gradient. *NeurIPS*, 33: 14254–14265, 2020. [1](#), [2](#), [6](#), [7](#), [12](#), [13](#)
- [37] Dmitry Ulyanov, Andrea Vedaldi, and Victor Lempitsky. Deep image prior. In *Proceedings of the IEEE conference on computer vision and pattern recognition*, pages 9446–9454, 2018. [5](#)
- [38] Yannick Verdie, Kwang Yi, Pascal Fua, and Vincent Lepetit. Tilde: A temporally invariant learned detector. In *CVPR*, pages 5279–5288, 2015. [6](#)
- [39] Changchang Wu. Towards linear-time incremental structure from motion. In *2013 International Conference on 3D Vision-3DV 2013*, pages 127–134. IEEE, 2013. [1](#)
- [40] Kwang Moo Yi, Eduard Trulls, Yuki Ono, Vincent Lepetit, Mathieu Salzmann, and Pascal Fua. Learning to find good correspondences. In *CVPR*, pages 2666–2674, 2018. [7](#), [8](#), [11](#), [12](#), [13](#), [14](#), [15](#), [16](#), [17](#), [18](#), [19](#)
- [41] Xu Zhang, Felix X Yu, Svebor Karaman, and Shih-Fu Chang. Learning discriminative and transformation covariant local feature detectors. In *CVPR*, pages 6818–6826, 2017. [6](#)
- [42] Qunjie Zhou, Torsten Sattler, and Laura Leal-Taixe. Patch2Pix: Epipolar-Guided Pixel-Level Correspondences. In *2021 IEEE/CVF Conference on Computer Vision and Pattern Recognition (CVPR)*, pages 4667–4676, Nashville, TN, USA, 2021. IEEE. [1](#)

Good Keypoints for the Two-View Geometry Estimation Problem

Supplementary Material

6. Generation of Synthetic Views

We define the distribution with PDF $p(\tilde{P}_i|\beta)$ by warping P_i with synthetic homographies, which are generated using a procedure from [6, 25]. The procedure produces a random homography $\tilde{\mathbf{H}}_i^\beta$ by solving for the transformation between a set of 4 fixed points and a set of 4 random points (see Fig. 4). The random points are obtained by perturbing the fixed points with three random variables sampled from the standard uniform distribution $\mathbf{Z}_1, \mathbf{Z}_2, \mathbf{Z}_3 \stackrel{\text{iid}}{\sim} \mathcal{U}(0, 1)$. The difficulty of generated homographies is controlled by β as illustrated in Fig. 4. Thus, denoting the procedure by G^β , a random homography $\tilde{\mathbf{H}}_i^\beta$ is obtained as:

$$\tilde{\mathbf{H}}_i^\beta = G^\beta(\mathbf{Z}_1, \mathbf{Z}_2, \mathbf{Z}_3). \quad (15)$$

Since not every homography is a plausible viewpoint transformation [6], the generated homographies are limited to perspective transformations, which are a special case of homographies. Given a random homography, a random patch \tilde{P}_i^β is obtained by applying a warping function W to the patch P_i :

$$\tilde{P}_i^\beta = W(P_i, \tilde{\mathbf{H}}_i^\beta). \quad (16)$$

See Fig. 5 for an example of a warped patch.

7. Training Details

We use subsets of MegaDepth [16] and IMC-PT [12] from [25] for training and validating our model. We keep the training hyperparameters and most of the parameters for generating the supervisory signal from NeSS-ST unchanged and train the model from scratch. We choose the new parameter as $t_{noise} = 0.0001$ and tune $\beta = 2.0$ on the validation subset of IMC-PT keeping it the same for all datasets during testing (see Table 5). BoNeSS-ST has the same U-Net architecture [27] as NeSS-ST and retains its fast training and inference time. The BoNeSS-ST model used in experiments in Sec. 4 and Sec. 9 was trained for 1 day and 5 hours on a single NVIDIA 3090 GPU, which is only slightly larger than the training time of NeSS-ST (22 hours on NVIDIA 2080 TI).

The design of the BoNeSS-ST detector was chosen via testing of component combinations that can be used for building a keypoint detector based on the stability score. Table 6 shows that detector variants utilizing $\mathbb{E}[\|\tilde{\mathbf{K}}_i - k_i\|_2]$ and $\sqrt{\text{tr}(\tilde{\Sigma}_i) + \tilde{\delta}_i^\top \tilde{\delta}_i}$ with $t_{salient}$, t_{noise} and Eq. 13 have equal performance on IMC-PT [12]. For this reason, we

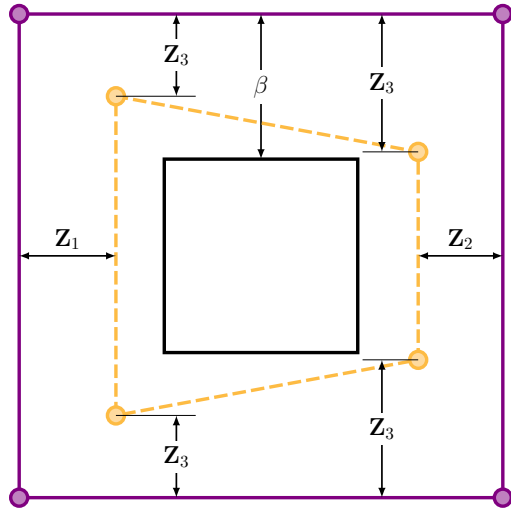


Figure 4. The homography generation procedure. Perturbed points (colored in yellow) are obtained by applying left, right and perspective displacements, which are controlled by \mathbf{Z}_1 , \mathbf{Z}_2 and \mathbf{Z}_3 respectively, to fixed points (colored in purple). β controls the magnitude of the displacements by preventing any of them from going inside the black square, which allows to regulate the difficulty of a generated homography.

additionally compared these models on ScanNet [5] (see Table 7). The model trained using $\sqrt{\text{tr}(\tilde{\Sigma}_i) + \tilde{\delta}_i^\top \tilde{\delta}_i}$ demonstrates the best overall performance.

Note, that the ablations in Table 3 and Table 4 are done on test sets and meant solely to support our claims in Sec. 4.3 and validate the proposed design choices of BoNeSS-ST with more data, which is crucial for having faithful mAA estimates. They were not used for choosing β and selecting the best design, which was done on validation sets as shown in this section (see Table 5, Table 6 and Table 7).

β	1.414	1.681	2.000	2.378	2.828	3.363
R	0.803	0.806	0.811	0.808	0.813	0.809
t	0.644	0.641	0.648	0.648	0.643	0.641

Table 5. Tuning β for BoNeSS-ST on the validation subset of IMC-PT. We report relative pose rotation (R) and translation (t) mAA [12, 40] for a 10-degree threshold. The best results are in red. Note, that the best values are selected according to a total sum of rotation and translation mAA.

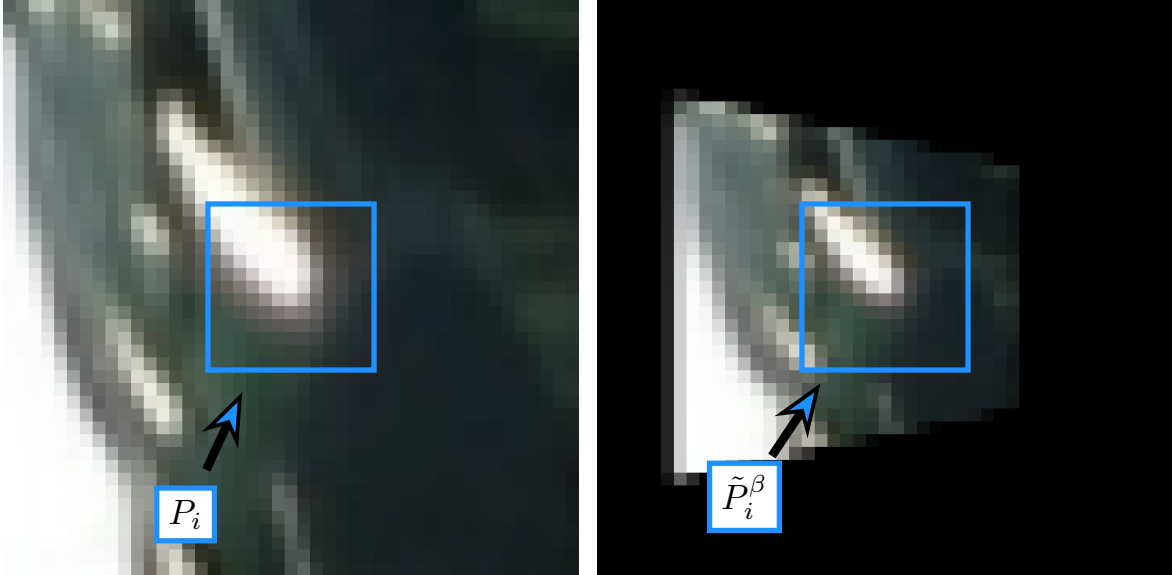


Figure 5. The effect of applying a homography generated according to Eq. 15 (see Fig. 4) to a part of an image. Since we use the Shi-Tomasi detector, the size of \tilde{P}_i^β , which is the realization of $\tilde{\mathbf{P}}_i^\beta$, that is required to procedure a single measurement is rather small - 13×13 pixels. So, warped patches can be generated fast with a reasonable GPU memory budget, enabling ground-truth generation during training.

β -EME	$t_{salient}$ [25]		$t_{salient}$ [25] + Eq. 13		$t_{salient}$ [25] + t_{noise}		$t_{salient}$ [25] + Eq. 13 + t_{noise}	
	R	t	R	t	R	t	R	t
$\ \bar{\Sigma}_i\ _2$ [25]	0.795	0.632	0.801	0.633	0.806	0.648	0.807	0.649
$\text{tr}(\bar{\Sigma}_i) + \bar{\delta}_i^\top \bar{\delta}_i$	0.800	0.635	0.796	0.638	0.806	0.649	0.806	0.645
$\sqrt{\text{tr}(\bar{\Sigma}_i) + \bar{\delta}_i^\top \bar{\delta}_i}$	0.788	0.633	0.796	0.635	0.805	0.648	0.811	0.648
$\mathbb{E}[\ \bar{\mathbf{K}}_i - k_i\ _2]$	0.796	0.633	0.799	0.640	0.809	0.646	0.811	0.648

Table 6. Selection of the best combination of design choices on the validation subset of IMC-PT [12]. We report rotation (R) and translation (t) mAA [12, 40] for a 10-degree threshold. The best results are in red. Note, that the best results are selected according to a total sum of rotation and translation mAA.

β -EME	$t_{salient}$ [25] + Eq. 13 + t_{noise}	
	R	t
$\sqrt{\text{tr}(\bar{\Sigma}_i) + \bar{\delta}_i^\top \bar{\delta}_i}$	0.586	0.198
$\mathbb{E}[\ \bar{\mathbf{K}}_i - k_i\ _2]$	0.567	0.187

Table 7. Selection of the best combination of design choices on the validation subset of ScanNet [5]. We report rotation (R) and translation (t) mAA [12, 40] for a 10-degree threshold. The best results are in red. Note, that the best results are selected according to a total sum of rotation and translation mAA.

8. Evaluation Protocol

There are three important factors that significantly influence the outcomes of the evaluation on the two-view geometry estimation task: (i) an image resolution [19], (ii) a keypoint budget [12] and (iii) hyperparameters of two-view geometry estimators [12]. In our work, we evaluate all methods using images in the original resolution [25] and choose the keypoint budget of 2048 keypoints as in [12, 25, 28, 36]. We estimate the two-view geometry using robust estimators listed in Table 9. To ensure a proper pick of hyperparameters for each method, we augment the hyperparameter tuning pipeline from [12, 25] with a grid search from [2]. Specifically, we choose initial values of hyperparameters via a greedy selection strategy [12] (see Fig. 6, Fig. 7 and Fig. 8). Next, we do a grid search in a small neighborhood

Method	HEB [2]		IMC-PT [12]		ScanNet [5]	
	Low ratio	Inlier threshold	Low ratio	Inlier threshold	Low ratio	Inlier threshold
SIFT [19]	1.0	2.6	0.99	0.7	0.96	2.2
SuperPoint [6]	1.0	2.8	0.98	1.0	0.93	2.8
R2D2 [26]	1.0	2.6	0.99	1.0	0.92	2.4
Key.Net [3]	1.0	3.0	1.0	1.2	0.95	2.2
DISK [36]	1.0	2.6	0.98	0.9	0.93	2.2
REKD [15]	1.0	3.0	0.98	1.4	0.91	2.4
Shi-Tomasi [31]	1.0	2.2	0.99	0.7	0.93	2.4
NeSS-ST [25]	1.0	2.6	0.98	0.7	0.91	2.4
BoNeSS-ST	1.0	3.0	0.99	0.7	0.92	2.4

Table 8. Final values of hyperparameters tuned using the grid search strategy [2].

around them as shown in Fig. 9. We do not provide plots like in Fig. 9 for all methods on all datasets since that would take a lot of space. Instead, we summarize the final values of tuned hyperparameters in Table 8.

Estimator	Dataset	Conf. level	Max. num. of iterations
DEGENSAC [4]	HEB [2]	0.9999	200000
	IMC-PT [12]		
	MegaDepth [16]		
OpenGV [14]	ScanNet [5]	0.9999	10000

Table 9. Two-view geometry estimators used in the evaluation in Sec. 4.1 and Sec. 9.1 and some of their hyperparameters.

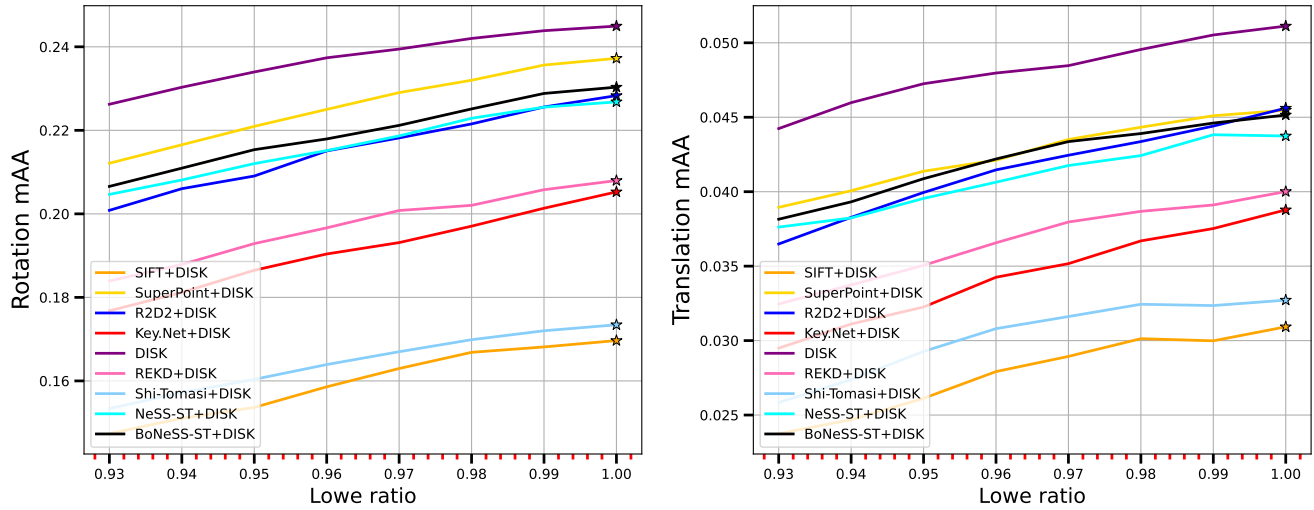
9. Additional Experiments

9.1. Evaluation on the Two-View Geometry Estimation Task

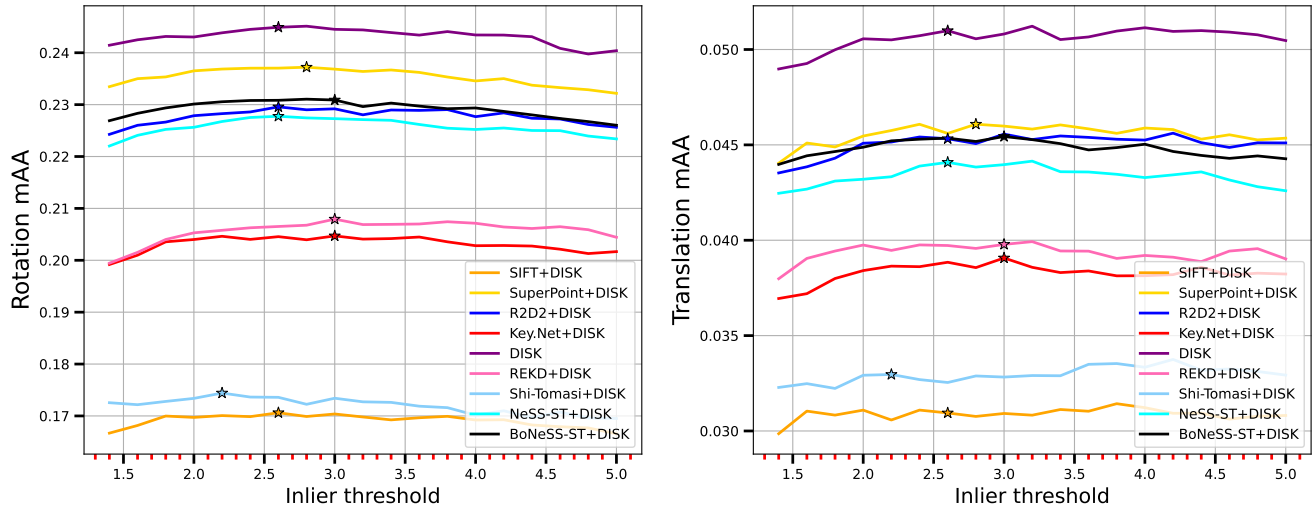
In Fig. 10, Fig. 11, Fig. 12 and Fig. 13, we provide relative pose accuracy-to-threshold curves [12, 40] based on which mAA values in Table 1 are calculated.

9.2. Evaluation with Classical Metrics

In Fig. 14, we supplement the results in Table 2 with repeatability [29] and MMA [7, 20] curves for all pixel thresholds.

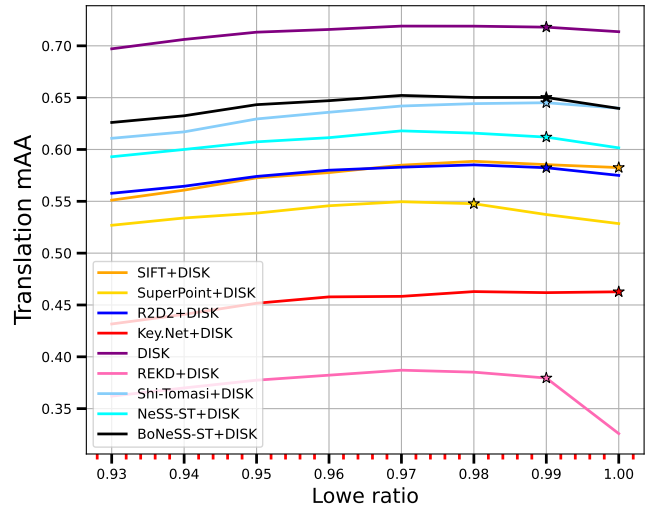
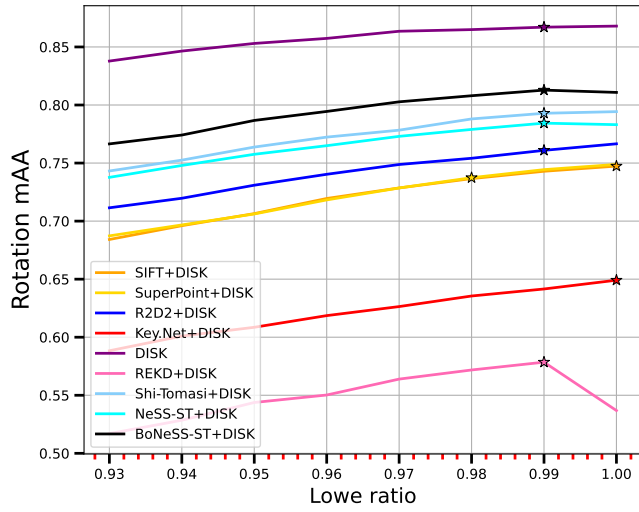


(a) Lowe ratio tuning.

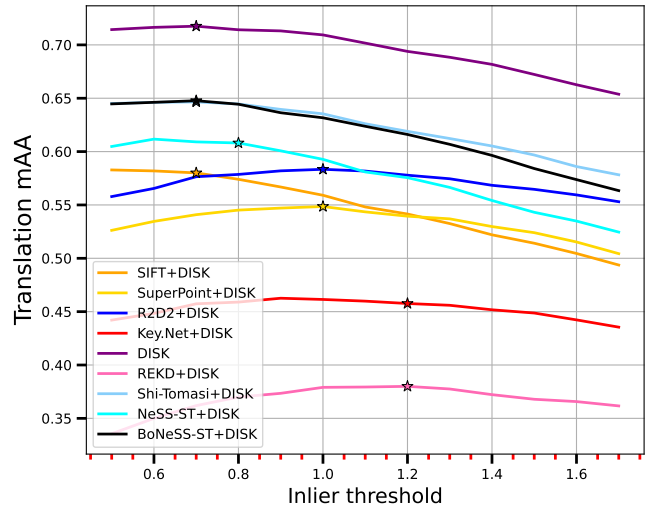
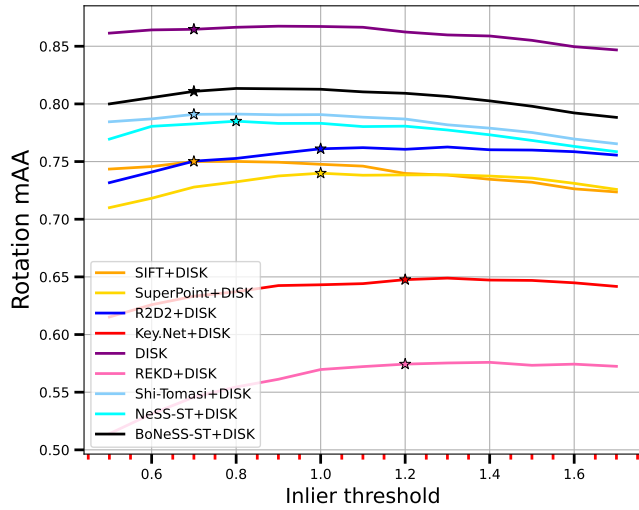


(b) Inlier threshold tuning.

Figure 6. Initial tuning of hyperparameters using the greedy strategy [12] on the validation subset of HEB [2]. We plot relative pose mAA-to-hyperparameter curves for rotation and translation. Stars mark the best hyperparameters according to the sum of rotation and translation mAA [12, 40].

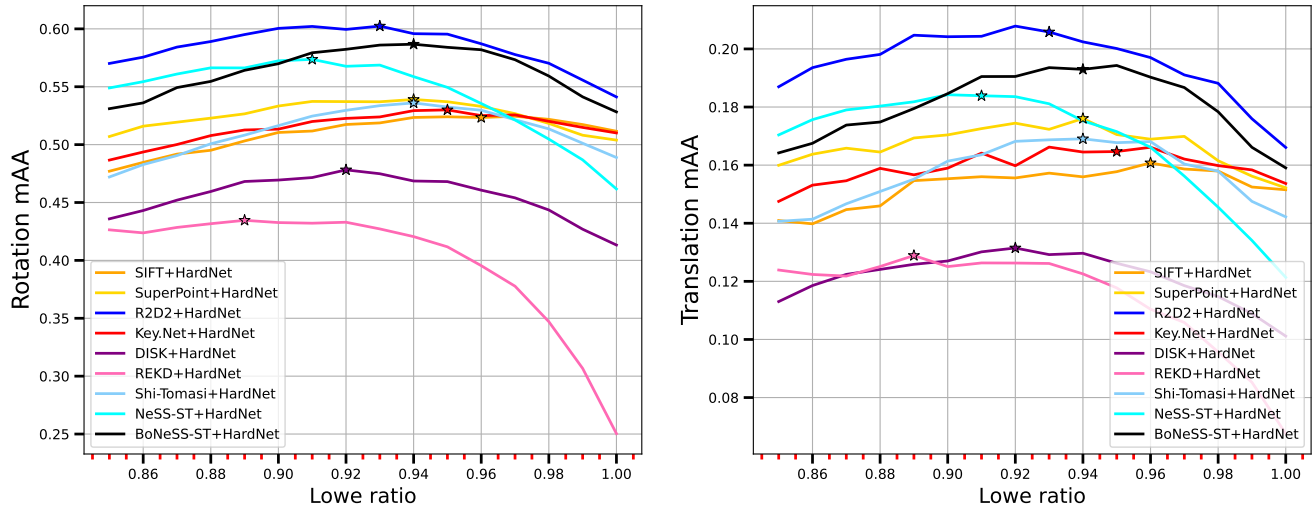


(a) Low ratio tuning.

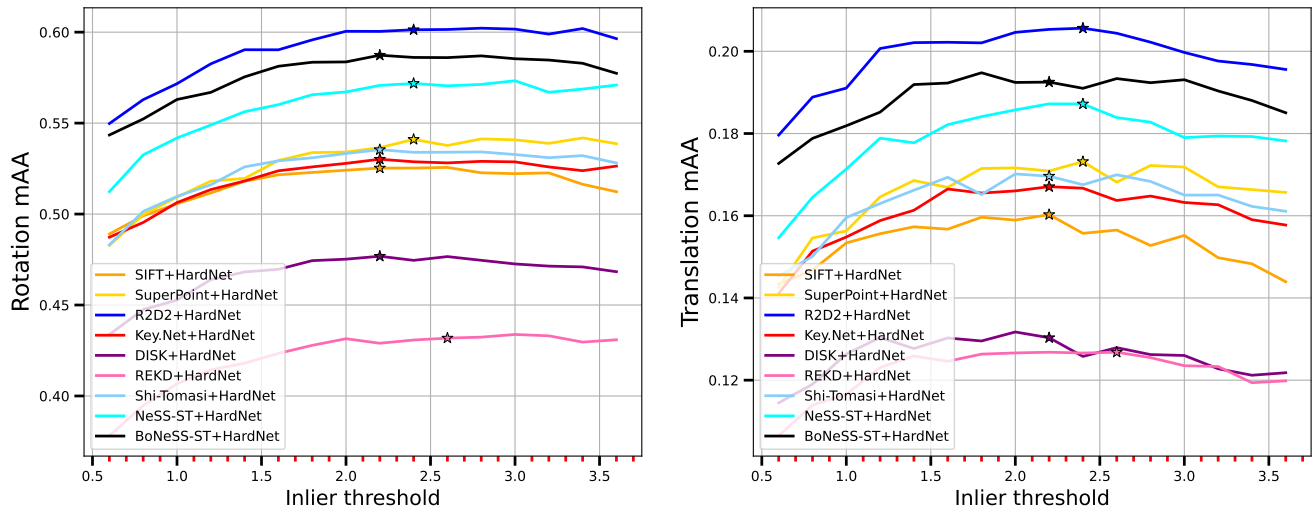


(b) Inlier threshold tuning.

Figure 7. Initial tuning of hyperparameters using the greedy strategy [12] on the validation subset of IMC-PT [12]. We plot relative pose mAA-to-hyperparameter curves for rotation and translation. Stars mark the best hyperparameters according to the sum of rotation and translation mAA [12, 40].



(a) Low ratio tuning.



(b) Inlier threshold tuning.

Figure 8. Initial tuning of hyperparameters using the greedy strategy [12] on the validation subset of ScanNet [5]. We plot relative pose mAA-to-hyperparameter curves for rotation and translation. Stars mark the best hyperparameters according to the sum of rotation and translation mAA [12, 40].

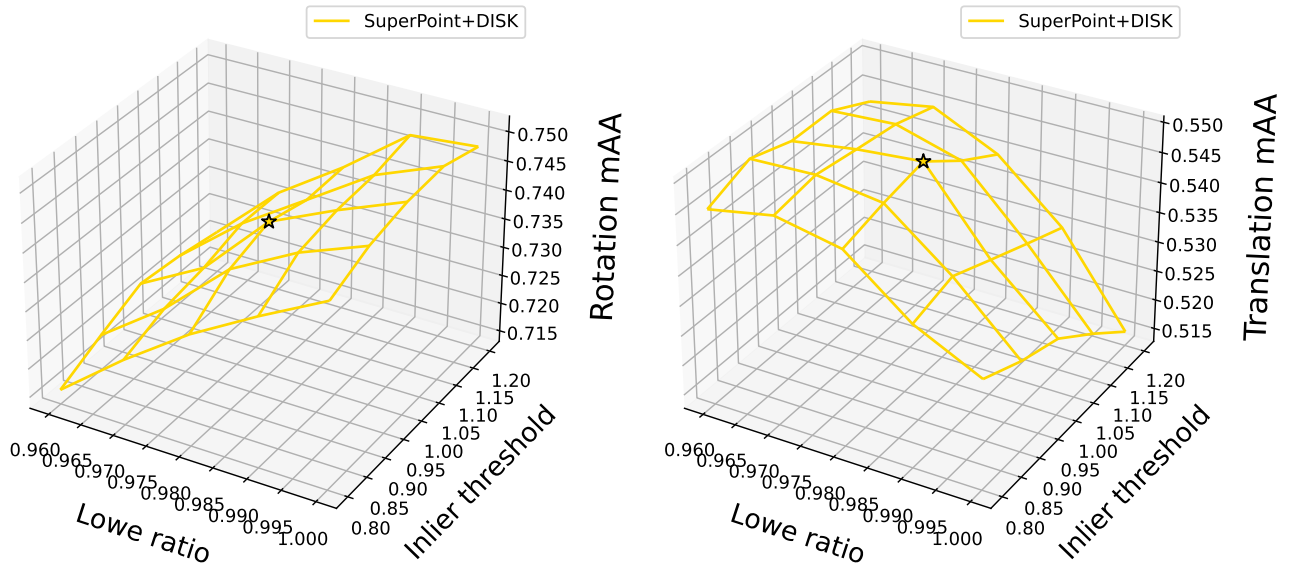


Figure 9. Grid search of hyperparameters on the validation subset of IMC-PT [12] for SuperPoint [6]. We plot relative pose mAA-to-hyperparameters grids for rotation and translation. Stars mark the best hyperparameters according to the sum of rotation and translation mAA [12, 40].

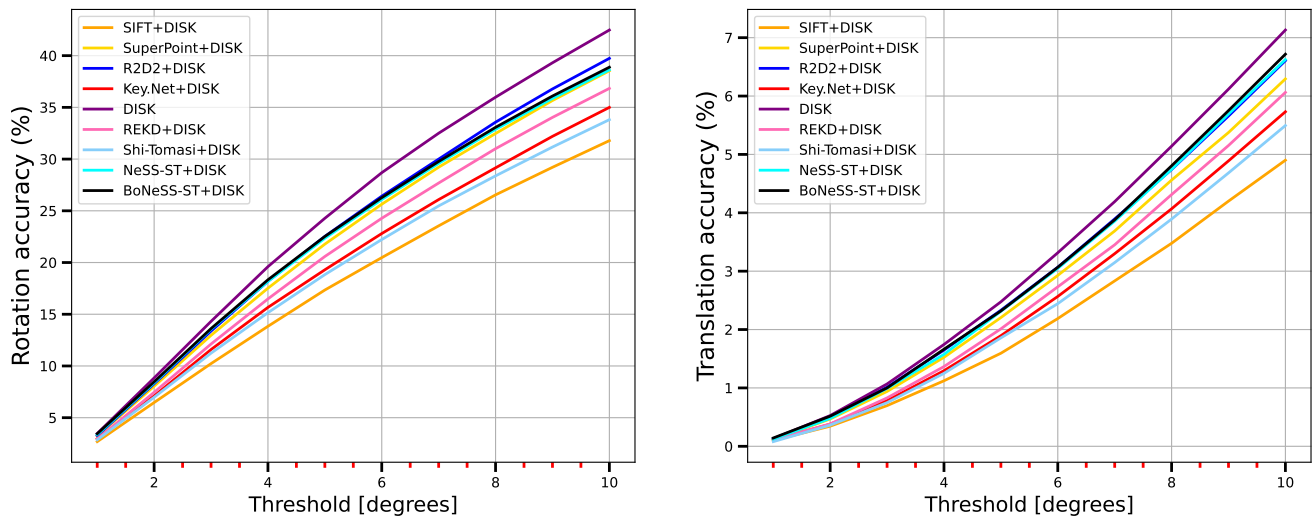


Figure 10. Evaluation on HEB [2] on the planar homography estimation task. We plot relative pose estimation accuracy-to-threshold curves for rotation and translation [12, 40].

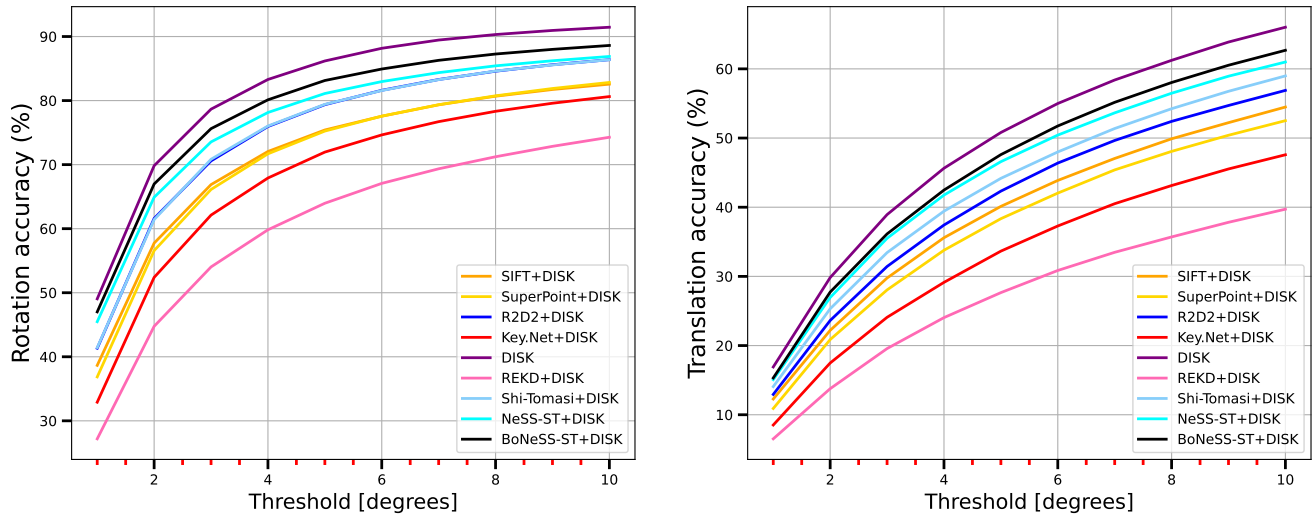


Figure 11. Evaluation on IMC-PT [12] on the fundamental matrix estimation task. We plot relative pose estimation accuracy-to-threshold curves for rotation and translation [12, 40].

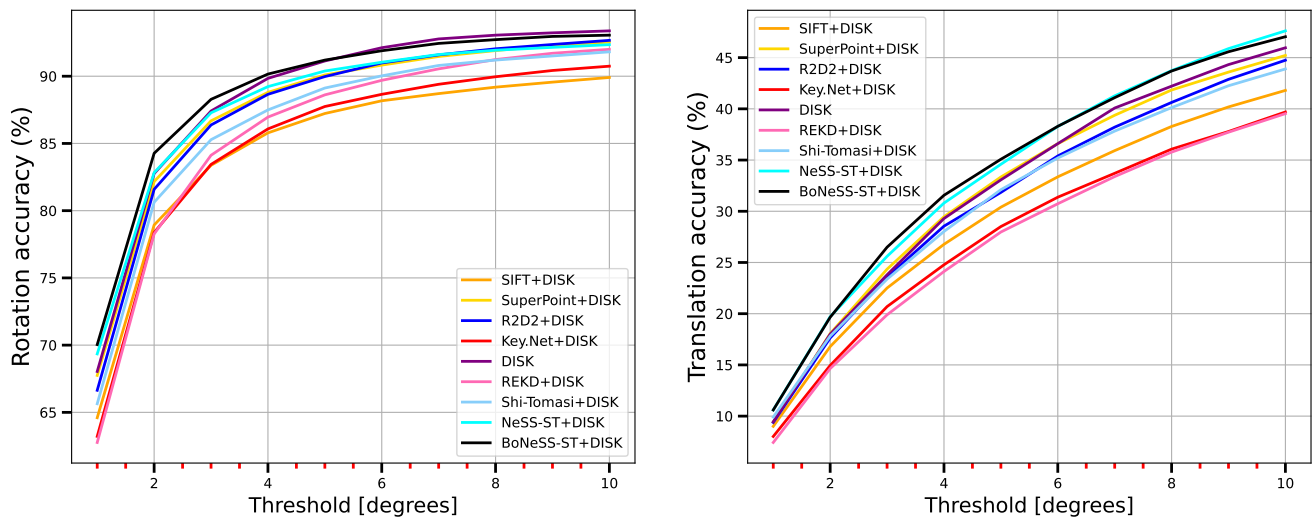


Figure 12. Evaluation on MegaDepth [16] on the fundamental matrix estimation task. We plot relative pose estimation accuracy-to-threshold curves for rotation and translation [12, 40].

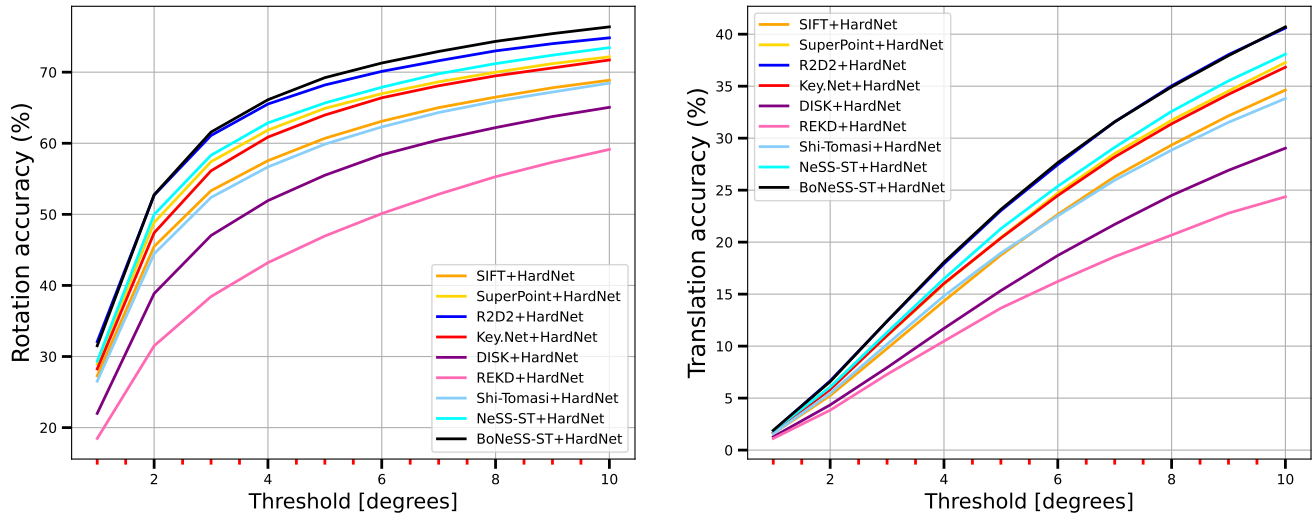
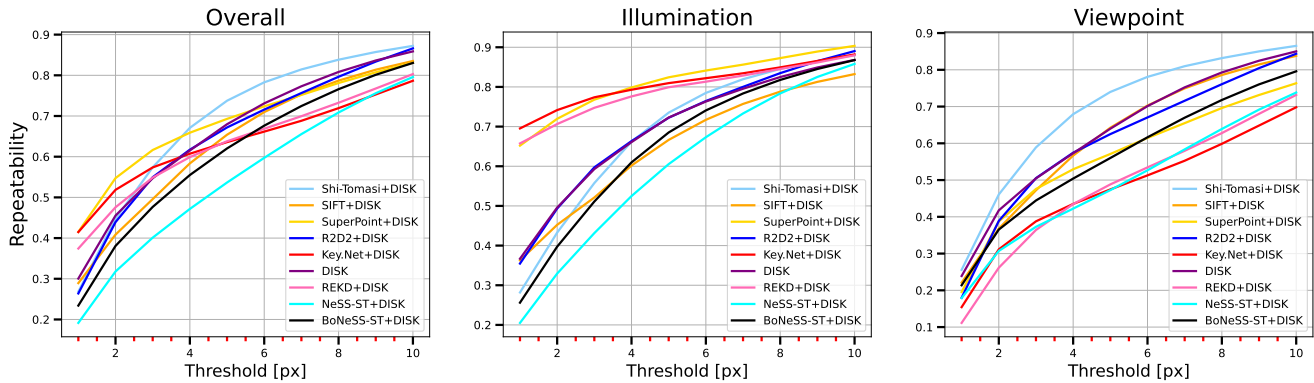
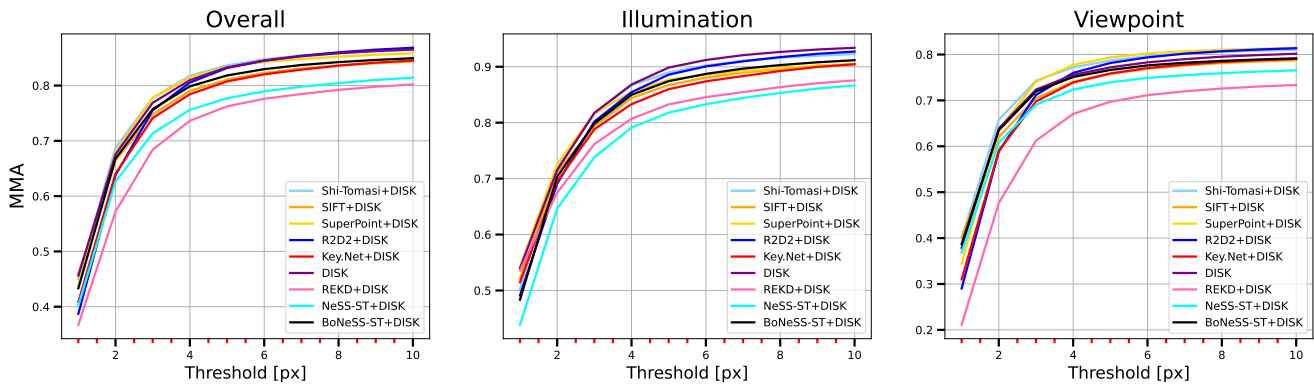


Figure 13. Evaluation on ScanNet [5] on the essential matrix estimation task. We plot relative pose estimation accuracy-to-threshold curves for rotation and translation [12, 40].



(a) We plot repeatability-to-threshold curves [29].



(b) We plot MMA-to-threshold curves [7, 20].

Figure 14. Evaluation on HPatches [1] using classical metrics.